CrystEngComm

Accepted Manuscript

Shape-controlled synthesis of three-dimensional triangular Bismuth microstructures and sensing of H_2O_2

Ashis Das and M. V. Sangaranarayanan[*]

Department of Chemistry, Indian Institute of Technology Madras Chennai-600036 India

*E-mail: sangara@iitm.ac.in

Tel: +91 44-22574209; Fax: +91 44-22570545

Abstract

The electrodeposition of triangular microstructures of Bi on Indium Tin Oxide surfaces is carried out by optimizing the potentials, precursor concentrations and deposition times. The potential-controlled hierarchical evolution of Bi geometries from triangles to dendrites is demonstrated and the structures have been characterized using SEM, TEM, AFM, XRD, UV Visible absorption and FT Raman spectroscopy. The Scharifker-Hills model is employed to elucidate the nucleation-growth mechanism of triangular Bi particles. The efficacy of Bismuth triangular structures towards the oxidation of H_2O_2 is analyzed using cyclic voltammetry and electrochemical impedance spectroscopy. From the Differential Pulse Voltammetry and chronoamperometry, Bi triangles coated Indium Tin Oxide is shown to be a satisfactory sensor for H_2O_2.

1. Introduction

In recent years, there has been growing interest on the synthesis of nanocrystalline semiconductors and semi-metals due to their unique physiochemical, mechanical and electrical properties which differ from those of typical noble and transition metals. Among these, Bismuth and its intermetallic alloys are of much interest due to their thermoelectric and superconducting properties. Bismuth exhibits unique optical and electronic properties due to its adjustable band gap, low charge carrier density, small effective mass, and large magnetoresistance effect.[1–6] Further, the bismuth modified electrodes have been explored as alternative to mercury electrodes due to their mechanical stability and catalytic properties.[7,8] Bismuth based electrodes have been extensively employed in electroanalysis for sensing of metal ions such as Zn^{2+}, Cd^{2+}, Pb^{2+} as well as pesticides and herbicides.[9] Due to the significance of hydrogen peroxide (H_2O_2) in biological systems and clinical applications, the development of efficient H_2O_2 sensors is essential. Furthermore, H_2O_2 participates in various enzyme-catalysed biochemical reactions and functions as a mediator in chemical and environmental processes.[10–13] Although the detection of H_2O_2 using Pt-based, carbon based, metal oxide electrodes has been studied [14–17], a simple, robust method is still lacking.

Since, the dimension and microstructure play a crucial role in determining physical properties of any material, various morphologies of Bi viz. hexagons,[18,19] wires,[20] spheres,[20–22] tubes,[23–25] cubes,[21] triangles,[26,21] and dendrites[27,28] have been synthesized using diverse processes such as electrochemical, solvothermal, hydrothermal, electron beam irradiation, electron beam lithography, vapor deposition etc. Among these techniques, electrodeposition has the advantages of fast synthesis time, simple operation and facile control of sizes, shapes and dimensions at ambient conditions.[29–31] The synthesis of bismuth triangular nanoplates has been reported using a thermal process in alkaline media with ascorbic acid as the reducing

agent in the presence of complexing agent (Na$_2$EDTA) and Polyvinylpyrrolidone (PVP).[26] Recently, the synthesis of diverse Bi nanostructures including triangular nanoplates has been reported using a polymer-assisted polyol process.[21] However, a facile and single step method for obtaining Bi triangular microstructures under surfactant-free and template-less conditions has been elusive.

In the present study, we report the synthesis of nano- and micro-sized bismuth triangular particles (Bi TPs) using a simple potentiostatic electrodeposition on Indium Tin Oxide (ITO) electrodes at room temperature. The shape-controlled synthesis is accomplished using low concentrations of the metal precursor and small cathodic potentials in conjunction with short deposition times. A hierarchical change in morphologies is effected by optimizing the potentials and time durations. The efficacy of the Bi TPs modified ITO electrodes for the sensing of H$_2$O$_2$ is also investigated using Differential Pulse Voltammetry and chronoamperometry.

2. Experimental

The synthesis of Bi triangular particles (Bi TPs) was carried out from the solution containing 10 mM Bi(NO$_3$)$_3$.5H$_2$O (Sigma–Aldrich, India) and 0.1 M HNO$_3$ (Merck, India) at room temperature (30 ± 1 ^{0}C). All other reagents of analytical grade potassium dihydrogen phosphate (KH$_2$PO$_4$), dipotassium hydrogen phosphate (K$_2$HPO$_4$), hydrogen peroxide (H$_2$O$_2$, 30%) and potassium ferricyanide (K$_3$Fe(CN)$_6$) from Fisher Scientific were used as received. The solutions were prepared using ultrapure water (18 MΩ, Milli-Q, Millipore). The electrochemical experiments were carried out using the CHI 660A electrochemical work station in a single-compartment glass cell with a three-electrode configuration consisting of a

3

Pt wire, Indium Tin Oxide (ITO) ($R_s \sim 25\ \Omega$) and Ag/AgCl (saturated KCl) as the counter, working, and reference electrode respectively. The electrodes were procured from CH instruments (USA). The ITO electrodes were cleaned with acetone and ultrapure water by sonication for 15 min to remove any adsorbed impurities. The electrochemical deposition was performed at various deposition potentials and time durations. After deposition, the electrodes were rinsed with deionized water and stored in desiccator for drying. All the potentials are reported here with reference to Ag/AgCl. The microstructures of bismuth deposits were characterized using scanning electron microscopy (SEM, FEI Quanta 400), transmission electron microscopy (TEM, Philips CM12), and atomic force microscopy (AFM, Dimension EDGE, Bruker). The crystallinity and purity of the deposits were studied using X-ray diffraction (XRD, Bruker D8), X-ray photoelectron spectrometer (XPS, SPECS, Germany) and FT-Raman spectroscopy with 488 nm excitation line of He–Ne laser using Horiba Jobin-Yvon (HR800 UV) micro-Raman spectrometer. The UV-Vis absorption spectra were obtained using Jasco V-650 spectrophotometer. The absorbance measurements of bismuth modified ITO electrode were carried out by placing the electrode inside the cuvette holder of the spectrophotometer. The sensing of H_2O_2 was carried out using differential pulse voltammetry (DPV) and chronoamperometry (CA) with Bi TPs modified ITO electrodes in 0.2 M phosphate buffer solution (PBS). All the voltammetric measurements were carried out with 10 mL volume of freshly prepared PBS (pH 7.2) supporting electrolyte. The DPV parameters were optimized as follows: amplitude = 0.05 V, pulse width = 0.06 s and pulse period = 0.5 s. Further, the chronoamperometric current was measured at a constant potential of 0.7 V for successive additions of 50 µL aliquot of 5 mM H_2O_2 with continuous stirring rate of 200 rpm. The Nyquist plots were obtained at the potential of 0.6 V in the frequency range of 10^5 Hz to 10^{-1} Hz with an amplitude of 5 mV.

3. Results and Discussion

3.1 Potentiostatic electrodeposition of Bi TPs

In order to deduce the optimum deposition potentials, a preliminary cyclic voltammetric study was carried out and Fig. 1(A) depicts a typical cyclic voltammogram of the ITO working electrode dipped in the solution of 0.01 M of $Bi(NO_3)_3$ and 0.10 M HNO_3. The chronoamperograms at various deposition potentials is depicted in Fig. 1(B).
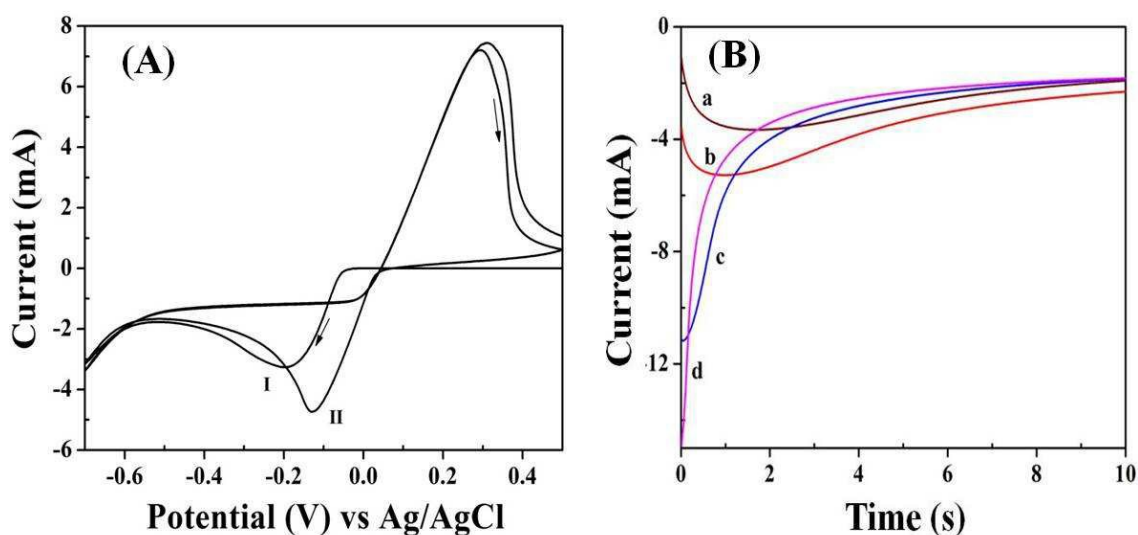

Fig. 1 (A) Cyclic Voltammograms of Bi deposition on the ITO electrode at a scan rate of 50 mV/s ; (I) and (II) denote respectively the first and second cycle and the potential is scanned from 0.45 V to -0.65V. (B) The chronoamperometric response at various deposition potentials: (a) -0.08 V, (b) -0.15 V, (c) -0.30 V and (d) -0.50 V.

The voltammetric response indicates the typical deposition – striping processes of Bi in acidic media and is consistent with earlier results.[32,33] In the following, we demonstrate how the controlled electrodeposition at low cathodic overvoltages and short time durations yields impressive morphologies. From the crossover potential of the first cycle, we infer that the cathodic deposition of Bi begins at a critical nucleation potential of -0.08 V. In contrast to conventional electrodeposition of Bi, at near-equilibrium potentials or high cathodic overpotentials, the deposition of Bi is carried out here using a single pulse potentiostatic approach with deposition times ranging 1 to 10s. This choice of short deposition times is deliberate so as to suppress any competing re-dissolution processes occurring in HNO_3 and to ensure a quasi steady-state.[18] Further, the density, geometry and dimensions of Bi nanocrystals were studied systematically at various nucleation potentials up to -0.5 V, while the concentration of the metal precursor and supporting electrolyte were also varied. The influence of the electrolyte concentration and deposition potential is shown in Table 1.

Table 1 Influence of deposition potentials and electrolyte concentrations on the morphologies of Bi for a deposition time of 10 seconds.

Concentration of $Bi(NO_3)_3$ (M)	Concentration of HNO_3 (M)	Deposition Potential (V)	Morphology
0.01	0.1	-0.15	Triangles
0.01	0.1	-0.30	Microspheres
0.01	0.1	-0.50	Tripods
0.05	1.0	-0.15	Hexagons
0.05	1.0	-0.30	Truncated hexagons along with dendrites
0.05	1.0	-0.50	dendrites

At higher cathodic overpotentials of -0.30 V and -0.50 V with same precursor concentrations and deposition times, the black shiny electrodeposits on ITO glass surface arise while the growth pattern changes to woolen bundle-like microspheres and subsequently to tripod shaped morphologies. Interestingly, the uniform hexagonal shaped Bi was obtained at a higher concentration of HNO_3 (1 M) and $Bi(NO_3)_3$ (0.05 M) at applied potential of -0.15 V. These high concentrations of the metal precursor and supporting electrolyte yield fern-shaped Bi dendrites, as was earlier reported using a two-step electrodeposition method.[27] Fig. 2 depicts the typical SEM, TEM and SAED images of Bi particles pertaining to various morphologies. With increase in the deposition time to 60s, micron-sized, non-uniform morphologies of polygonal shapes are formed. (Fig. S1, ESI)
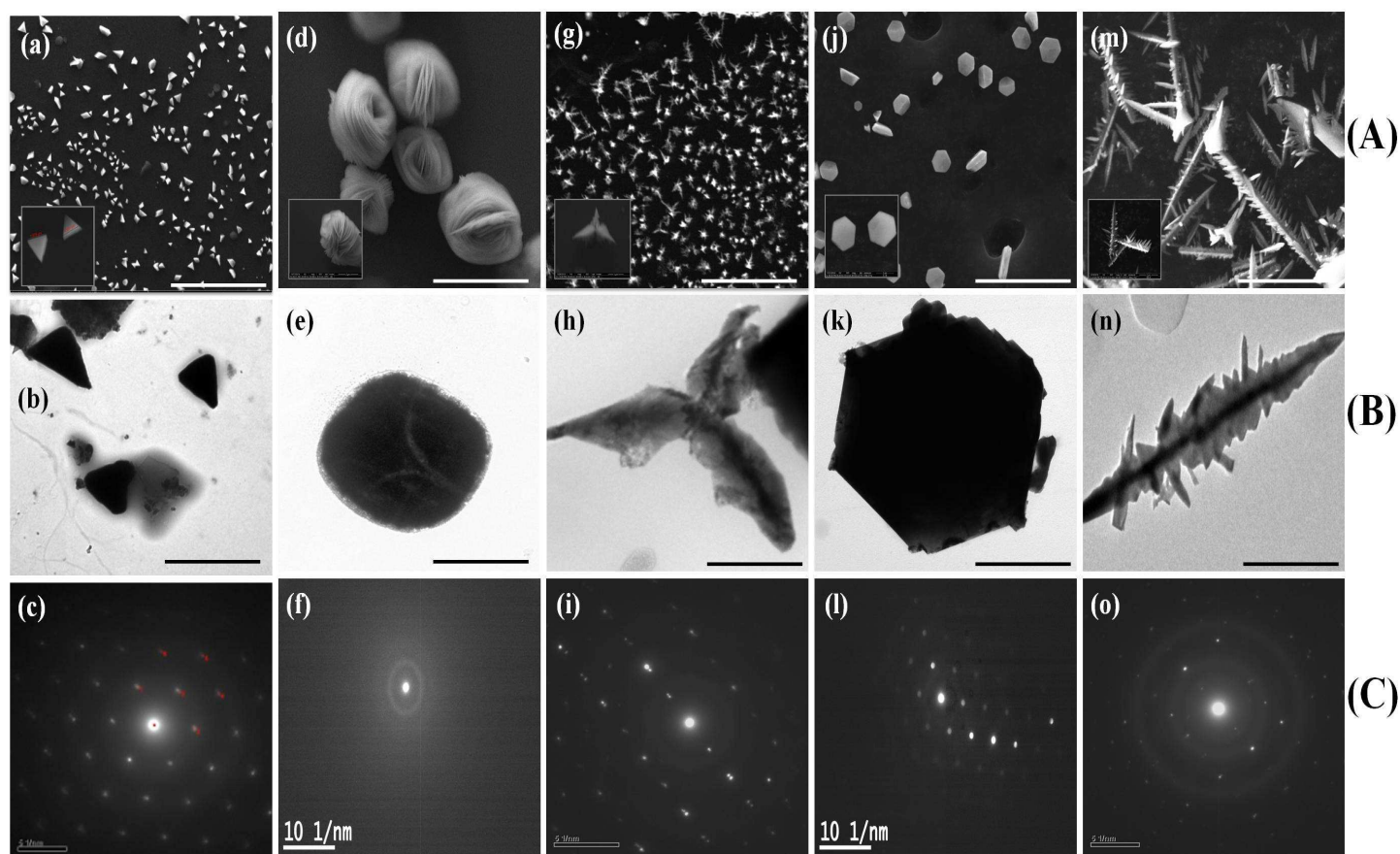
Fig. 2 Typical SEM (A), TEM (B) and SAED (C) images of various Bi microstructures; triangles (a-c), spheres (d-f), tripods (g-i), hexagons (j-l) and dendrites (m-o). The scale bar represents 10 µm for SEM and 1 µm for TEM images.

The SEM images for Bi TPs depicted in Fig. 2a reveal an uniform distribution of Bi particles without any agglomeration. The triangular geometry of Bi is predominant along with other polygonal shapes. The higher magnification images shown in the inset of Fig. 2a imply that the edges of triangular shaped particles vary from *ca.* 500 nm to 2 µm. However, the Bi TPs of mean particle size of 150 nm are formed when 1 mM of $Bi(NO_3)_3$ is employed. (Fig. S1, ESI) The XRD pattern for Bi TPs indicated in the Fig. 3b can be indexed to the hexagonal rhombohedral phase (JCPDS 05-0519) of bismuth with the major peaks assigned to (012), (112), (202) and (024) planes. The peak positions and intensities are in agreement with the known values of the cell parameters a = 4.545 A^0 and c = 11.83 A^0. Furthermore, the other morphologies of Bi have analogous diffraction characteristics. (Fig. S2, ESI) The SAED pattern (Fig. 2c) of triangular Bi nanoparticles indicates the crystalline nature of bismuth while the hexagonal symmetry of the diffracted spots confirms the single crystalline nature of Bi nanotriangle bounded by (001) facets.[26] The strongest intensity diffraction spots are caused by reflection from (104) plane and the outer weaker intensity spots from (220) plane with respective lattice spacing of 0.237 nm and 0.136 nm.
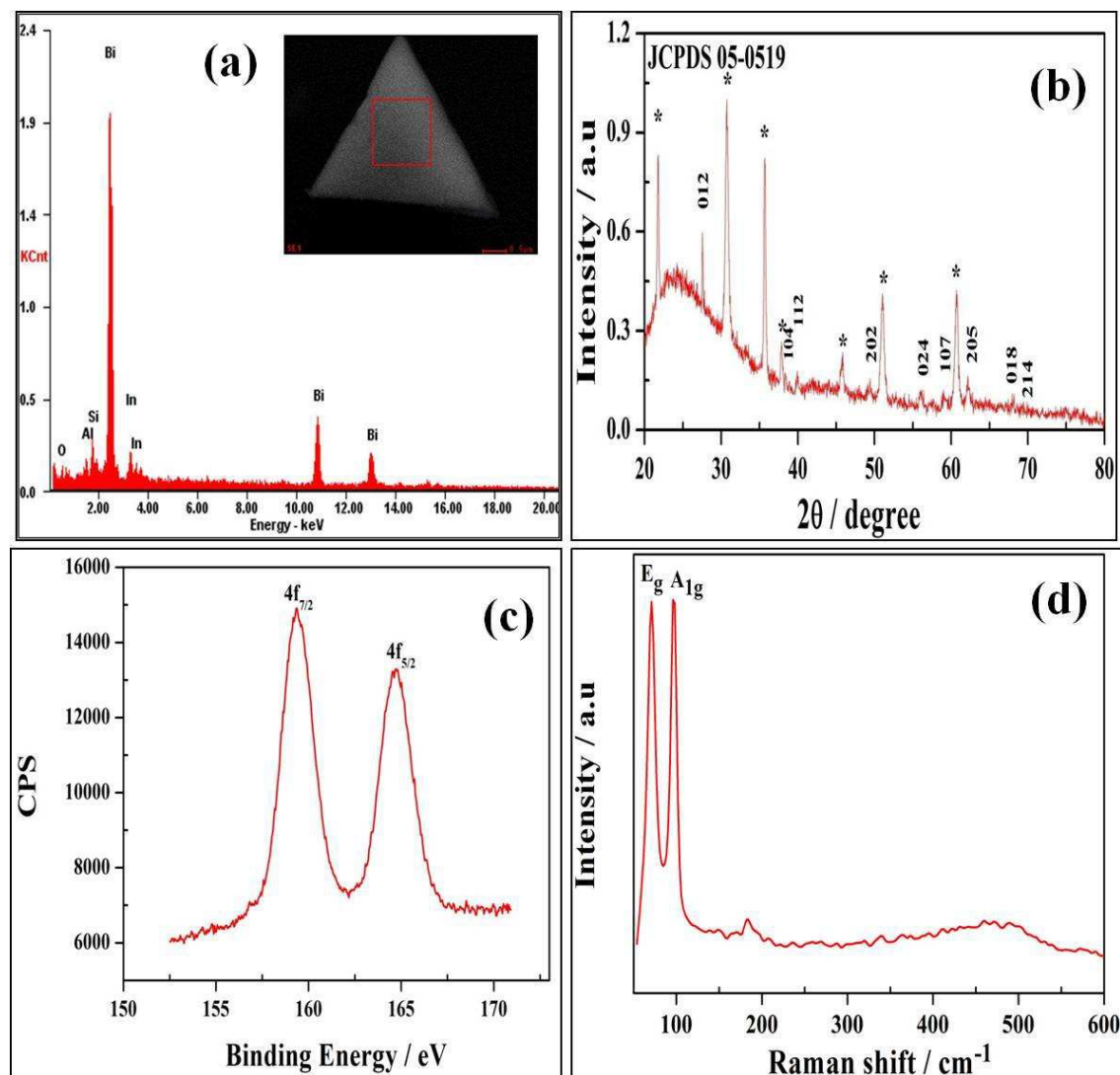
Fig. 3 (a) EDAX , (b) XRD, (c) XPS and (d) FT-Raman spectrum of Bi TPs. The asterisks in (b) denote the XRD pattern of the bare ITO surface.

The HRTEM image depicted in the inset of Fig. 4b confirms the single crystal nanoplates with fringe spacing of 0.227 nm. The measured lattice spacing of the plane corresponds to the (110) plane of rhombohedral Bi. The topographical images obtained from the AFM images are depicted in Figs. 4c and 4d. The smooth nature of the surface with homogeneously distributed particles is inferred from the AFM results. The surface roughness is estimated as

0.126 μm from the root mean square (RMS) based upon the Z-range values. The composition

of the deposits inferred from the EDAX spectrum shown in Fig. 3a indicates 37 weight % of

Bi. Further, the XPS data of Bi TPs is depicted in Fig. 3c. wherefrom the peaks at 158.2 and

164.1 eV confirm the $4f_{7/2}$ and $4f_{5/2}$ core levels of Bi, thereby indicating a high purity.[34] The

Raman scattering bands at 69.9 and 97.1 cm^{-1} for the Bi TPs (Fig. 3d) are attributed to the

first order scattering E_g and A_{1g} modes of metallic Bi.[18] Further, the typical Raman spectra

for various morphologies of Bi microstructures have been compared to analyze the structural

change of Bi. (Fig. S3, ESI) The appearance of Raman bands at about 120 nm and 310 nm for

Bi hexagons, tripods and dendrites respectively correspond to the Raman signature of oxide

layer (α-Bi_2O_3) along with the underlying bismuth metal.[35] However, the exposure of high

power laser leads to the disintegration of Bi particles. (Fig. S4, ESI)
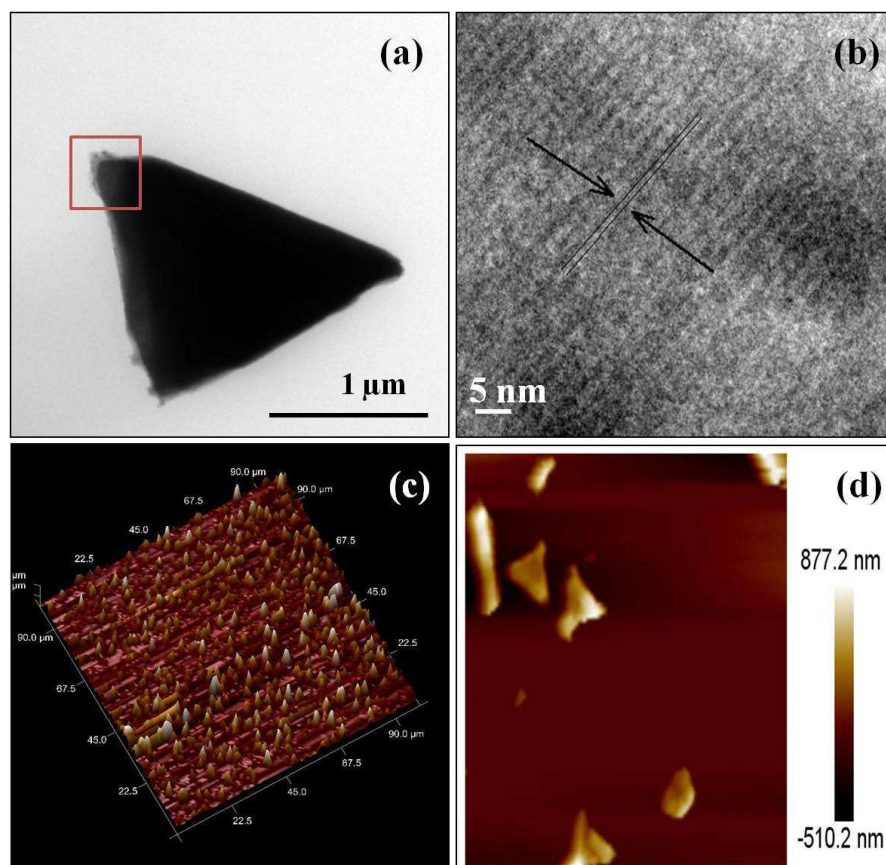
Fig. 4 (a) TEM image of Bi TP and (b) HRTEM image of the area indicated in (a); (c) and (d) AFM images of Bi TPs.
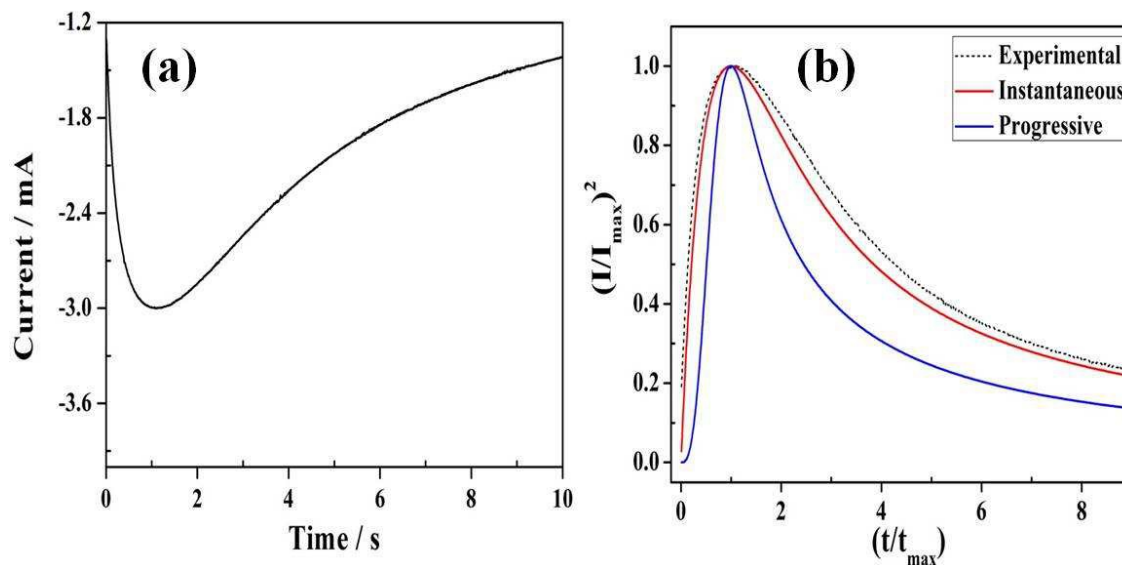
3.2 Nucleation and Growth mechanism of Bi TPs

The Scharifker-Hills model plays an important role in the elucidation of the nucleation mechanism for constructing theoretical non-dimensional current transients. It has no empirical fitting parameters and requires the maximum current and corresponding time as the input parameters. Hence it has been extensively employed in distinguishing instantaneous and progressive nucleation growth models for electrodeposition.[36] In this study, we analyse the prediction of the SH model for the formation of Bi TPs on ITO. The governing eqns for the two nucleation mechanisms are given below:

Instantaneous:
$$\left(\frac{I}{I_{max}}\right)^2 = \frac{1.9542}{\frac{t}{t_{max}}}\left\{1 - \exp\left(-1.2564\frac{t}{t_{max}}\right)\right\}^2 \tag{1}$$

Progressive:
$$\left(\frac{I}{I_{max}}\right)^2 = \frac{1.2254}{\frac{t}{t_{max}}}\left\{1 - \exp\left[-2.3367\left(\frac{t}{t_{max}}\right)^2\right]\right\}^2 \tag{2}$$

where I and I_{max} denote the current at time t and t_{max} respectively.

11

Fig. 5 (a) The experimental current–time transient for the deposition of Bi TPs at -0.15 V and (b) the corresponding non-dimensional plots for elucidating the nucleation-growth mechanism.

As seen from Fig. 5(b), the experimental curve fits satisfactorily with theoretical instantaneous nucleation curve ensuring the three-dimensional growth of Bi TPs on ITO. This corresponds to the slow growth of Bi nuclei on a small number of active sites simultaneously. The uniform size distribution of Bi TPs evinced from the AFM studies shown in Fig. 4c also validates the instantaneous nucleation mechanism. The number density of the nucleation sites is calculated using the equation:[37]

$$N_0 = 0.0652 \frac{1}{(8\pi cM/\rho)^{1/2}} \frac{(zFc)^2}{i_{max}^2 t_{max}^2} \tag{3}$$

where z corresponds to the number of electrons (3), F denotes the Faraday's constant (96485 C mol^{-1}), c denotes the bulk concentration of the electrolyte (1×10^{-5} mol cm^{-3}) and M is the

molar mass of the Bi (208.98 g mol^{-1}), ρ being its density (9.78 g cm^{-3}). Hence in the case of the instantaneous nucleation mode, the apparent number of nucleation site density N_0 follows as 9.39×10^5 cm^{-2}. Further, the number density of the deposited atoms increases when the potential is more negative than -0.15 V. The number of apparent nucleation sites ($\sim 10^5$ cm^{-2}) is consistent with reported literature as obtained from analysis of chronoamperometric transients.[38]
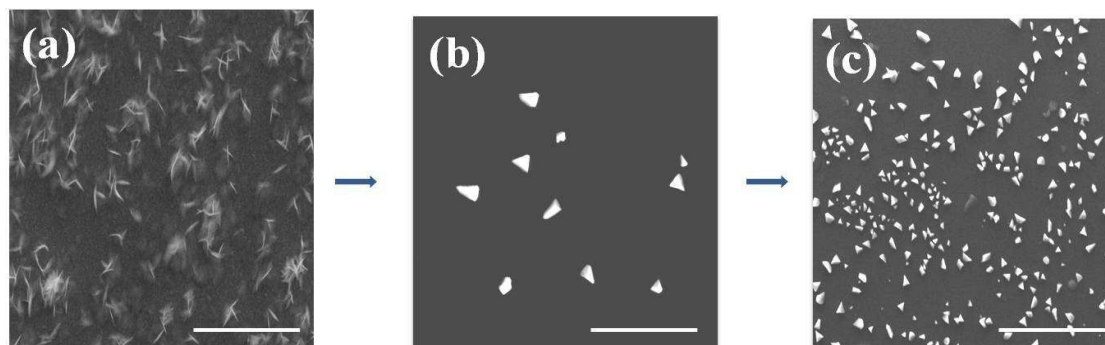
Fig. 6 Typical SEM images of triangular bismuth particles obtained using the deposition potential of -0.15 V for different durations: (a) 1s, (b) 5s and (c) 10s. The scale bar represents 10 µm. Other conditions as in Fig. 1.

The lower magnitude of the cathodic overpotentials and the concentration of the electrolyte play an important role in controlling various morphologies. In order to elucidate the mechanism of the crystal growth of triangular Bi nanoparticles on polycrystalline ITO electrode, we have carried out the deposition at different time intervals ranging from 1s to 10s. Fig. 6 depicts the SEM images at different deposition times for the optimal potential of -0.15 V. It is seen from Fig. 6a that the bismuth particles form platelets-like structures at deposition time of 1s. When the deposition time increases to 10s, the nano-seeds aggregate together to yield triangular shaped particles and with further increase to 60s, non-uniform polygonal microstructures arise. A schematic illustration for the proposed growth mechanism

of bismuth triangular nanoparticles is shown in Fig. 7. The shape-controlled growth of triangular Bi morphologies can be comprehended from the thermodynamic and kinetic considerations.[19] Since, the composition of each Bi triangle particle is inferred to be single crystalline, from the thermodynamic perceptive, the driving force for the spontaneous oriented attachment of Bi nano-seeds (shown in scheme 7) are assumed to be predominantly electrostatic interactions between ions and van der waals forces between planes.[39] As a result, this leads to the elimination of pairs of high energy surfaces to stable triangle geometry. The surface energies of different crystallographic planes are different. Because of the large surface-to-volume ratio of the nano-sized particles, the relative reduction of Bi^{3+} compete with that of NO_3^- ions and the potential-dependent diffusion of bismuth adatoms influence the growth of crystal.[19] Both the diffusion rate and the reduction kinetics influence the rate-determining steps for particle formation. From the chemical kinetics aspects, the observed growth pattern suggests that the lower migration potentials, deposition times and optimal electrolyte concentrations minimize the rate of diffusion and hence the triangular shaped geometries arise. In the case of lower concentration of electrolyte, the Bi^{3+} ions diffusing to the electrode get reduced immediately resulting in the formation of triangular Bi particles. However, the increase in the concentration of HNO_3 and $Bi(NO_3)_3$ lead to the oriented attachments followed by the self-assembly which alters the growth pattern into micron-sized bundle-like sphere, tripods, hexagons and dendritic bismuth particles. In addition to the controlled diffusion and reduction rate of Bi^{3+} ions, the role of ITO substrate has a significant effect on the formation of different morphologies of Bi nanoparticles as a result of its active grain boundaries. Although the other electrodes such as Cu, BDD, Pt, GC, Au etc. have been employed to yield different morphologies of Bi, the triangular morphology of Bi here is solely facilitated due to the instantaneous nucleation mechanism on the ITO surface aiding the slower growth of bismuth crystals.
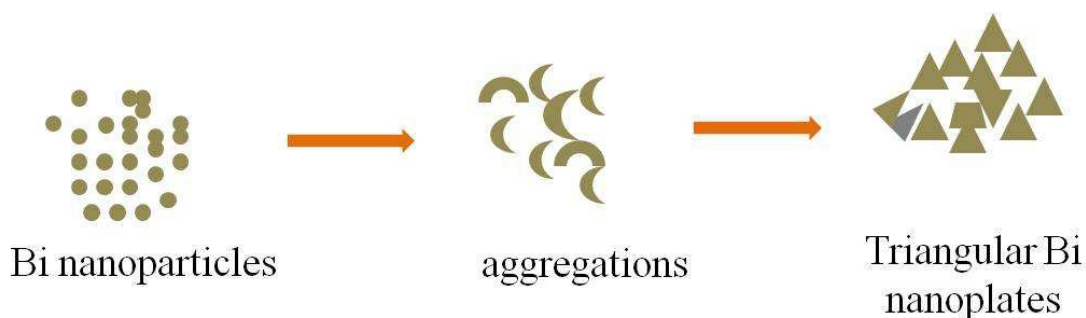
Fig. 7 Schematic depiction of the growth mechanism of Bi TPs.

3.3 Optical properties of Bi TPs

It is of interest to investigate the optical properties of bismuth nanoparticles arising from the surface plasmon resonance characteristics. It has been demonstrated that these bands for metals are influenced significantly by the morphologies than on the sizes.[40] The absorption spectrum of the Bi TPs deposited ITO electrode is depicted in Fig. 8 and exhibits three resonance bands corresponding to three polarizability axes of nanoparticles. A high intense band around 334 nm and a less intense band around 445 nm indicate respectively the out-of-plane dipolar and quadrupole excitation for bismuth nanostructures.[41,42] While the broad absorption band around 676 nm is associated with the in-plane dipole plasmon resonance corresponding to the longitudinal resonance. Upon comparison with the absorption spectra of different shapes of bismuth deposits, the high intense bands for the triangular Bi particles might be attributed due to the anisotropy shape. On the other hand, the single absorption band for hexagonal shaped Bi appears at 375 nm while no prominent peaks are observed in the case of dendrites. (Fig. S5, ESI)
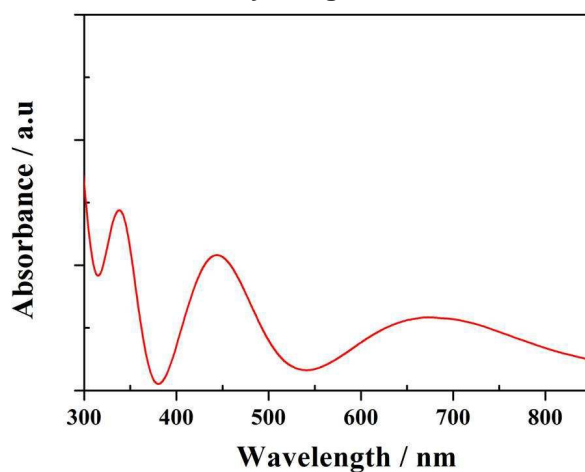
Fig. 8 UV-Vis absorption spectrum of Bi TPs.

4. Application to sensing of H$_2$O$_2$

Hydrogen peroxide is an important electroactive molecule which can exhibits either oxidation or reduction via direct electron transfer at solid electrodes as depicted in below:

$$H_2O_2 \rightarrow 2H^+ + O_2 + 2e^-$$ (5)

$$H_2O_2 + 2H^+ + 2e^- \rightarrow 2H_2O$$ (6)

In analytical applications, the detection of H$_2$O$_2$ has been focused on modified electrodes in order to decrease the overpotential and increase the electron transfer kinetics. In order to analyze the efficacy of different morphologies of Bi modified ITO electrodes for sensing of H$_2$O$_2$, preliminary DPV studies were carried out using 0.2 M PBS solution. (Fig. S6, ESI) We observed an enhancement in the sensitivity and peak current for triangular Bi deposits in comparison with other morphologies of Bi and further, the Bi TPs modified electrode depicts significantly higher current than *bulk* Bi on ITO electrode. (Fig. S7, ESI) Thus emphasizing the influence of the nanostructure on the sensing behavior, the triangular Bi modified ITO electrode was chosen as the working electrode. We have estimated the active surface area of the Bi TP modified ITO electrode using cyclic voltammetry with K$_3$Fe(CN)$_6$ as the redox

probe. The active surface area of the electrode is calculated from Randles-Sevcik equation as follows:[43]

$$i_p = (2.69 \times 10^5)n^{3/2}A.c_b.D^{1/2}.v^{1/2} \qquad (7)$$

where i_p corresponds to the anodic peak current, n is the number of electrons (n=1), c_b is the bulk concentration (0.01 M) and D denotes the diffusion coefficient (0.76×10^{-5} cm^2 s^{-1}) of $[Fe(CN)_6]^{3-}$ anion , v being the scan rate (V s^{-1}). From the linear variation of the peak current with the square root of the scan rate, the active surface area is estimated as 0.358 cm^2. (Fig. S8, ESI) Hence, the current response for Bi modified ITO electrode is normalized with respect to the active surface area.

The voltammetric and impedimetric response for 1 mM H_2O_2 in 0.2 M PBS at Bi TPs modified ITO electrode is shown in Fig. 9. The cyclic voltammogram in Fig. 9a compares the electrocatalytic behavior of Bi TPs coated surface with the bare ITO electrode in 0.2 M phosphate buffer solution (pH 7.2) containing 1 mM of H_2O_2. The onset potential pertaining to the electrooxidation of H_2O_2 occurs at 0.45 V, indicating a significant decrease in the overpotential for the modified electrode. The increase in the anodic peak current for Bi TPs modified ITO towards H_2O_2 oxidation is due to increase in the diffusion rate of the H_2O_2 towards the electrode surface.
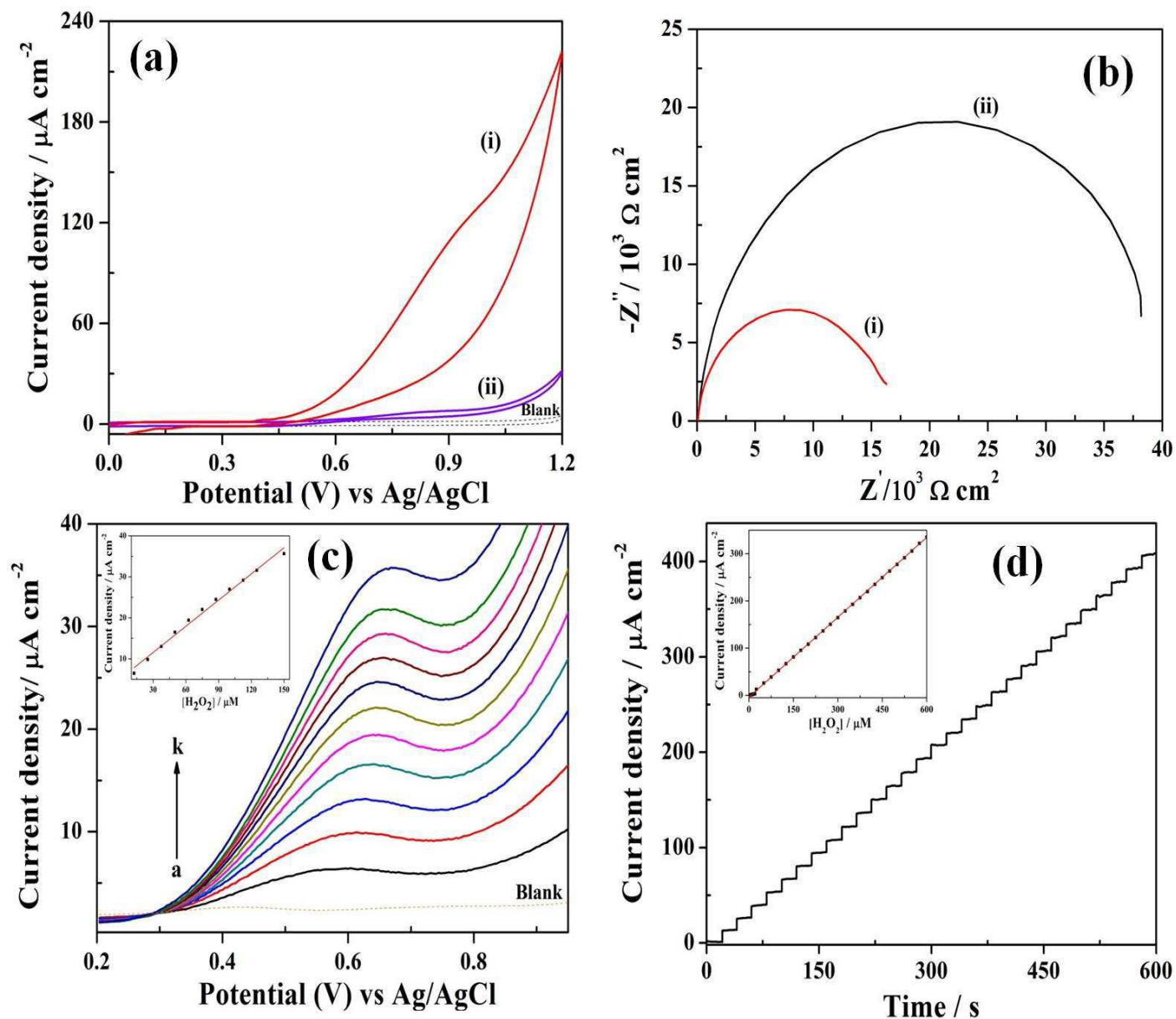
Fig. 9 (a) Cyclic voltammograms and (b) Nyquist plots of (i) Bi modified ITO and (ii) bare ITO in 0.2 M PBS electrolyte containing 1 mM of H_2O_2; (c) Differential pulse voltammograms and (d) amperometric current responses of triangular Bi modified ITO electrode at various concentrations of H_2O_2. The insets in (c) and (d) depict the linear calibration plot ranging from 12 to 150 µM and 25 to 750 µM respectively. The scan rate in (a) is 50 mV/s.

Further, the Nyquist plots in Fig. 9b provide an estimate of the charge transfer resistance (R_{CT}) from which the exchange current density (i_0) for the oxidation of H_2O_2 can be deduced as follows:

$$R_{CT} = \frac{RT}{nFi_0} \qquad (8)$$

The exchange current density (i_0) is calculated by using eq. 8 as R = 8.314 J K^{-1} mol^{-1}, T = 298 K, n = 2, F = 96485 C mol^{-1} and R_{CT} = 1.62 × 10^4 Ω. The charge transfer resistance (R_{CT}) of Bi modified electrode (R_{CT} = 1.62 × 10^4 Ω) is nearly three times smaller than the bare electrode (R_{CT} = 4.19 × 10^4 Ω) and on account of the inverse relation between R_{CT} and i_0, the Bi triangles modified ITO has a larger exchange current density of 2.21 μA/cm^2.

In order to examine the feasibility of triangular Bi modified ITO electrodes for sensing of H_2O_2, the differential pulse voltammetric and amperometric measurements were performed to elucidate the sensitivity and limit of detection. Fig. 9c depicts the DPV response for continuous additions of 20 μL of 5 mM H_2O_2 stock solution. In the chronoamperometric response (Fig. 9d), a linear dependence of the steady state current with successive additions of H_2O_2 is observed with the sensitivity of 0.564 μA μM^{-1} cm^{-2} and a linear range of 25-750 μM. The lowest detection limit (LOD) is estimated as 5 μM using the signal to noise (S/N) ratio as 3. The response of Bi modified ITO also shows the reproducibility upto 10 repetitive voltammetric measurements of 1 mM hydrogen peroxide concentration with relative standard deviation (RSD) of ~ 2%. However, the current response decreases presumably due to the fouling of the electrode.

The electrochemical detection of H2O2 using chemically modified electrodes have been an extensively investigated area of research in view of its importance in environmental and analytical chemistry. Among various nanoparticles (NP's)- modified electrodes

investigated in this context, the following deserve mention: Ag NP's coated glassy carbon[10,] Cu NP's coated polyethylene terephthalate[44] , multi-walled carbon nanotubes modified by electrochemical co-deposition of copper and silicomolybdate [45] and Fe_2O_3 NP's coated glassy carbon [46] each of them having μM limit of detection. On the other hand, Pt NP's decorated graphene-carbon nanotube hybrid paper electrode provides nanomolar detection [47]. While the present method has also led to μM detection limit, the preparation of the electrode is simple and facile. Furthermore, the voltammetric and impedimetric methods have been employed for sensing of H_2O_2 .

5. Conclusions

We have demonstrated a simple potentiostatic deposition method to obtain triangular bismuth microparticles on ITO surfaces and elucidated the growth mechanism with the help of the Scharifker-Hills model in support with extensive SEM studies. A hierarchical evolution of other morphologies of bismuth is demonstrated by optimizing the precursor concentrations and applied potentials. The Bi-modified electrode is shown to be an efficient non-enzymatic sensor for H_2O_2. The improved performance of Bi-modified electrode is ascribed to the unique electronic structure and properties of triangular Bi. Further studies are essential for the bulk synthesis of highly uniform triangular bismuth nanocrystals.

Acknowledgements

References

1.   J. Mangez, H. J, Issi, P. J, and Heremans, *Phys. Rev. B*, 1976, **14**, 4381–4385.

2. Y. Lin, S. B. Cronin, J. Y. Ying, M. S. Dresselhaus, and J. P. Heremans, *Appl. Phys. Lett.*, 2000, **76**, 3944–3946.

3. Y. Hasegawa, Y. Ishikawa, T. Saso, H. Shirai, H. Morita, T. Komine, and H. Nakamura, *Phys. B*, 2006, **382**, 140–146.

4. D. Kim, S. Lee, J. Kim, and G. Lee, *Appl. Surf. Sci.*, 2006, **252**, 3525–3531.

5. L. Li, Y. Yang, X. Fang, M. Kong, G. Li, and L. Zhang, *Solid State Commun.*, 2007, **141**, 492–496.

6. B. O. Brien, M. Plaza, L. Y. Zhu, L. Perez, C. L. Chien, and P. C. Searson, *J. Phys. Chem. C*, 2008, **112**, 12018–12023.

7. C. Prior, S. B. Hoc, I. Svancara, and J. Wang, *Electroanalysis*, 2010, **22**, 1405–1420.

8. N. Reim, A. Littig, D. Behn, and A. Mews, *J. Am. Chem. Soc.*, 2013, **135**, 18520–18527.

9. C. A. De Lima and A. Spinelli, *Electrochim. Acta*, 2013, **107**, 542–548.

10. C. M. Welch, C. E. Banks, a. O. Simm, and R. G. Compton, *Anal. Bioanal. Chem.*, 2005, **382**, 12–21.

11. B. Wang, J. J. Zhang, Z. Y. Pan, X. Q. Tao, and H. S. Wang, *Biosens. Bioelectron.*, 2009, **24**, 1141–1145.

12. E. Gómez-Plaza and M. Cano-López, *Food Chem.*, 2011, **127**, 1835–1835.

13. W. Chen, S. Cai, Q.-Q. Ren, W. Wen, and Y.-D. Zhao, *Analyst*, 2012, **137**, 49–58.

14. S. H. Chang, M. H. Yeh, J. Rick, W. N. Su, D. G. Liu, J. F. Lee, C. C. Liu, and B. J. Hwang, *Sensors Actuators, B Chem.*, 2014, **190**, 55–60.

15. W. J. Lin, C. S. Liao, J. H. Jhang, and Y. C. Tsai, *Electrochem. commun.*, 2009, **11**, 2153–2156.

16. H. Kivrak, O. Alal, and D. Atbas, *Electrochim. Acta*, 2015, **176**, 497–503.

17. X. Yin, M. Guo, Y. Xia, W. Huang, and Z. Li, *J. Electroanal. Chem.*, 2014, **720-721**, 19–23.

18. T. Som, A. Simo, R. Fenger, G. V Troppenz, R. Bansen, N. Pfänder, F. Emmerling, J. Rappich, T. Boeck, and K. Rademann, *Chemphyschem*, 2012, **13**, 2162–2169.

19. A. R. Rajamani, U. B. R. Ragula, N. Kothurkar, and M. Rangarajan, *CrystEngComm*, 2014, **16**, 2032–2038.

20. J. Wang, X. Wang, Q. Peng, and Y. Li, *Inorg. Chem.*, 2004, **43**, 7552–7556.

21. W. Z. Wang, B. Poudel, Y. Ma, and Z. F. Ren, *J. Phys. Chem. B*, 2006, **110**, 25702–25706.

22. H. Safardoust-Hojaghan, M. Salavati-Niasari, M. H. Motaghedifard, and S. M. Hosseinpour-Mashkani, *New J. Chem.*, 2015, **39**, 4676–4684.

23. R. Boldt, M. Kaiser, D. Ko, F. Krumeich, and M. Ruck, *Nano Lett.*, 2010, **10**, 208–210.

24. S. Derrouiche, C. Z. Loebick, and L. Pfefferle, *J. Phys. Chem. C*, 2010, **114**, 3431–3440.

25. D. Yang, G. Meng, Q. Xu, F. Han, M. Kong, and L. Zhang, *J. Phys. Chem. C*, 2008, **112**, 8614–8616.

26. F. Ruiling, X. Shu, L. Yi-Nong, and Z. Jun-Jie, *Cryst. growth Des.*, 2005, **5**, 1379–1385.

27. M. Yang, *J. Mater. Chem*, 2011, **21**, 3119–3124.

28. Y. Ni, Y. Zhang, and J. Hong, *CrystEngComm*, 2011, **13**, 794–799.

29. M. Tsai and T. Yeh, *Electrochem. commun.*, 2006, **8**, 1445–1452.

30. X. Chen, N. Li, K. Eckhard, L. Stoica, W. Xia, J. Assmann, M. Muhler, and W. Schuhmann, *Electrochem. commun.*, 2007, **9**, 1348–1354.

31.   M. Sun, G. Zangari, M. Shamsuzzoha, and R. M. Metzger, *Appl. Phys. Lett.*, 2001, **78**, 2964–2966.

32.   E. Sandnes, M. E. Williams, U. Bertocci, M. D. Vaudin, and G. R. Stafford, *Electrochim. Acta*, 2007, **52**, 6221–6228.

33.   M. Yang and Z. Hu, *J. Electroanal. Chem.*, 2005, **583**, 46–55.

34.   M. Wang, Z. Hong, and G. Xiong, *Supercond. Sci. Technol.*, 1997, **10**, 304.

35.   K. Trentelman, *J. Raman Spectrosc.*, 2009, **40**, 585–589.

36.   B. Scharifker and G. Hills, *Electrochim. Acta*, 1983, **28**, 879–889.

37.   G. Gunawardena, G. Hills, I. Montenegro, and B. Scharifker, *J. Electroanal. Chem. Interfacial Electrochem.*, 1982, **138**, 225–239.

38.   S. C. S. Lai, R. A. Lazenby, P. M. Kirkman, and P. R. Unwin, *Chem. Sci.*, 2015, **6**, 1126–1138.

39.   J. F. Banfield, S. a Welch, H. Zhang, T. T. Ebert, and R. L. Penn, *Science*, 2000, **289**, 751–754.

40.   Y. Yu, S. Chang, C. Lee, and C. R. C. Wang, *J. Phys. Chem. B*, 1997, **101**, 6661–6664.

41.   M. Peng, C. Zollfrank, and L. Wondraczek, *J.Phys Condens. Matter*, 2009, **285106**, 1–6.

42.   A. N. Romanov, Z. T. Fattakhova, D. M. Zhigunov, V. N. Korchak, and V. B. Sulimov, *Opt. Mater. (Amst).*, 2011, **33**, 631–634.

43.   A. J. Bard and L. R. Faulkner, *Electrochemical methods Fundamentals and Applications*, John Wiley & Sons Inc, Second., 2001.

44.   Eunju Kim,Narayanasamy Sabari Arul, Liu Yang and Jeong In Han, RSC Advances., 2015, **5**, 76729-76732.

45.   Kuo-Chiang Lin, Ying-Hui Chen, Shen-Ming Chen InT.j.Electrochem.Sci 2015, **10** ,

9205-9215.

46. Chen Hao, Yuru Shen, Zhiyuan Wang,Xiaohang Wang,Feng Feng, Cunwang Ge,Yutao Zhao and Kun Wang ACS sustainable Chemistry and Engineering 2015(in Press).

47.   Y.Sun, K.He, Z .Zhang ,A. Zhou and H.Duan Biosens Bioelectron., 2015 , **68**, 358-364.

Bi TPs modified ITO

$$H_2O_2$$

$$2H^+ + O_2 + 2e^-$$

1

2